

Multivalency-Induced Shape Deformation of Nanoscale Lipid Vesicles: Size-Dependent Membrane Bending Effects

Hyeonjin Park, Tun Naw Sut, Bo Kyeong Yoon, Vladimir P. Zhdanov, Jin Woong Kim, Nam-Joon Cho,* and Joshua A. Jackman*



Cite This: *J. Phys. Chem. Lett.* 2022, 13, 1480–1488



Read Online

ACCESS |



Metrics & More

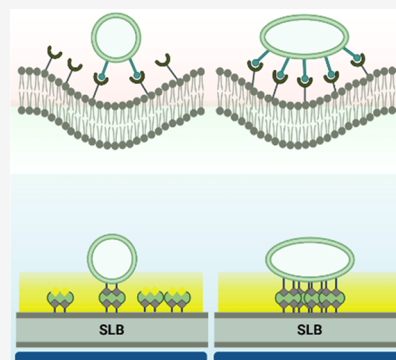


Article Recommendations



Supporting Information

ABSTRACT: The size of membrane-enveloped virus particles, exosomes, and lipid vesicles strongly impacts functional properties in biological and applied contexts. Multivalent ligand–receptor interactions involving nanoparticle shape deformation are critical to such functions, yet the corresponding effect of nanoparticle size remains largely elusive. Herein, using an indirect nanoplasmonic sensing approach, we investigated how the nanoscale size properties of ligand-modified lipid vesicles affect real-time binding interactions, especially vesicle deformation processes, with a receptor-modified, cell membrane-mimicking platform. Together with theoretical analyses, our findings reveal a pronounced, size-dependent transition in the membrane bending properties of nanoscale lipid vesicles between 60 and 180 nm in diameter. For smaller vesicles, a large membrane bending energy enhanced vesicle stiffness while the osmotic pressure energy was the dominant modulating factor for larger, less stiff vesicles. These findings advance our fundamental understanding of how nanoparticle size affects multivalency-induced nanoparticle shape deformation and can provide guidance for the design of biomimetic nanoparticles with tailored nanomechanical properties.



The functions of membrane-enveloped biological nanoparticles such as exosomes^{1,2} and virus particles^{3,4} along with synthetic ligand-functionalized vesicles^{5,6} and lipid nanoparticles (LNPs)^{7,8} often depend on multivalent ligand–receptor interactions with cell membrane surfaces. For example, exosome attachment to cellular membranes is an important step in diverse biological processes, including cellular signaling,⁹ immune responses,¹⁰ and cancer progression.¹¹ In addition, the multivalent binding of virus particles to cell membrane receptors can affect the degree of virus transmissibility.¹² Recently, there has been heightened interest in not only understanding the fundamental biology of these nanoparticle–membrane interactions but also elucidating key nanoparticle design parameters that can be utilized to develop more effective nanoparticle-based vaccines, therapeutics, and diagnostics.^{7,8} For example, LNPs and synthetic lipid vesicles have been increasingly used for vaccine and drug delivery applications,^{7,8} and it has been observed that their properties such as size and membrane composition can influence membrane fusion, cellular internalization, and/or immunogenicity.^{13,14}

Experimentally, fluid-phase lipid vesicles have served as simple models of nanoscale membrane curvature, and researchers have sought to understand how membrane stiffness depends on deformation-related changes in the membrane bending energy and osmotic pressure.^{15,16} These nanoscale deformation effects have been mainly studied by depositing lipid vesicles onto a flat, polyelectrolyte-coated substrate and

measuring indentation properties by atomic force microscopy (AFM). Early studies in the field demonstrated that deformation-induced osmotic pressure was a key contributing factor to membrane stiffness whereby fluid-phase lipid vesicles became stiffer as the osmotic pressure increased due to vesicle deformation.^{17,18} In such studies, it is usually implicitly assumed that the membrane bending rigidity, a quantitative parameter related to membrane bending energy, is an intrinsic property of vesicles with a particular composition and that the corresponding modulus is independent of vesicle size. Other studies have focused on more heterogeneous, cell-derived biological nanoparticles (e.g., exosomes and extracellular vesicles) and further demonstrated that the bending modulus can be influenced by (i) vesicular contents such as the lipid composition and the type and amount of membrane-associated proteins^{19,20} and (ii) nanoparticle size.²¹ In the latter case, it was reported that larger extracellular vesicles tended to have less stiff membranes because of smaller membrane bending energy and osmotic pressure.²¹

Received: January 12, 2022

Accepted: February 3, 2022



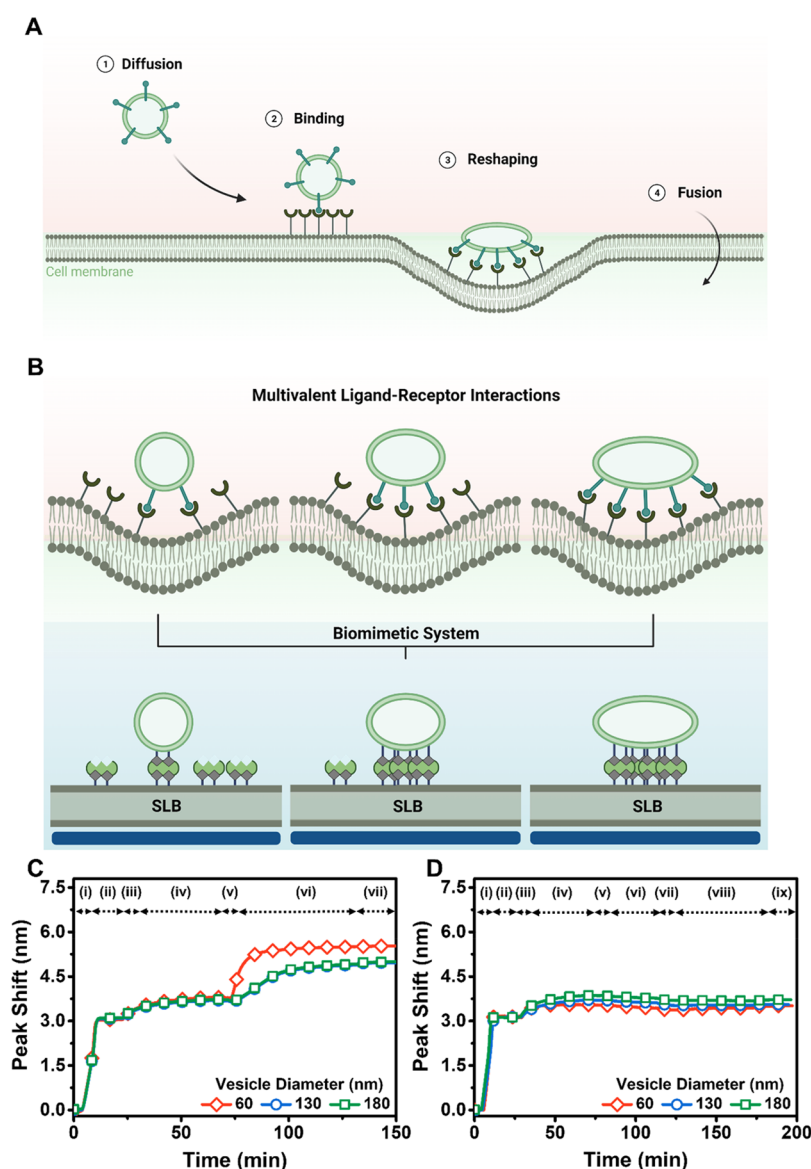


Figure 1. Biophysical concept of nanoparticle size-dependent multivalent binding interactions and experimental strategy. (A) Schematic illustration of how a ligand-modified, membrane-enveloped nanoparticle binds multivalently to cell surface receptors according to (1) diffusion, (2) binding, (3) reshaping, and (4) internalization (via fusion or endocytosis). (B) Schematic illustration of receptor-mediated binding of ligand-modified nanoparticles (vesicles in our case) to cell surface receptors as a function of nanoparticle size (top) and the corresponding experimental platform based on tracking the attachment of different-size, biotinylated lipid vesicles to an SLB platform bearing membrane-associated streptavidin protein receptors (bottom). In general, when the biotin ligand density in vesicles is relatively low, there can be some empty biotin-binding sites still available on streptavidin receptors, whereas these receptor sites are fully occupied when the biotin ligand density in vesicles is higher. Hence, the number of biotin–streptavidin bond pairs at the vesicle–SLB interface can be varied depending on the ligand density. At very high biotin ligand densities in the vesicles, there can be an excess of biotin ligands, in which case the number of biotin–streptavidin bond pairs is alternatively determined by the streptavidin receptor density in the SLB. (C) Representative LSPR $\Delta\lambda_{\max}$ shift responses tracking the attachment of different-size biotinylated lipid vesicles to a streptavidin-functionalized SLB surface. In the representative experiments, the SLB and vesicles both contained 1 mol % biotin. The baseline signals were initially established in (i) a buffer solution, followed by (ii) bicelle addition and SLB fabrication, (iii) a rinsing step, (iv) streptavidin protein attachment, (v) another rinsing step, (vi) vesicle attachment, and (vii) a final rinsing step. (D) Corresponding LSPR $\Delta\lambda_{\max}$ shifts for control experiments to confirm that the attachment of biotinylated lipid vesicles relies on specific biotin–streptavidin interactions. Steps (i–v) were conducted as described for panel C, and then (vi) free biotin was added to bind to membrane-associated streptavidin receptors, followed by (vii) a rinsing step, (viii) vesicle attachment, and (ix) another rinsing step.

However, to date, relevant studies have been focused on the deformation of lipid vesicles and exosomes attached to substrates via nonspecific electrostatic attraction, and size-dependent studies within the scope have utilized cell-derived vesicles that have inherent heterogeneity. There is an outstanding need to improve our biophysical understanding of the attachment-related deformation of nanoscale lipid

vesicles to the more biologically relevant context of specific, multivalent ligand–receptor interactions and to elucidate how nanoparticle size might affect such interactions.

To address this question, herein, we have controlled the nanoscale size properties of ligand-modified, fluid-phase lipid vesicles and scrutinized how vesicle size affects receptor-mediated vesicle attachment to and resulting deformation on a

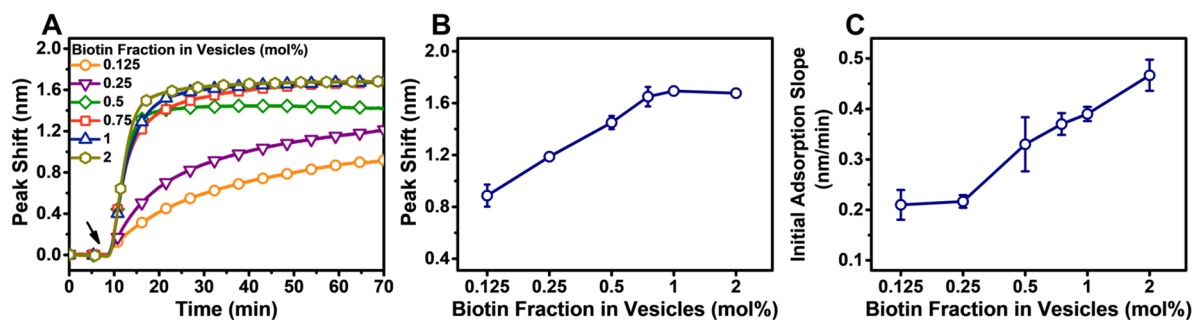


Figure 2. LSPR measurements tracking the attachment of 60 nm diameter, ligand-functionalized vesicles to receptor-functionalized SLBs. (A) Time-dependent $\Delta\lambda_{\max}$ shifts corresponding to attachment of biotinylated lipid vesicles to an SLB for different biotin ligand densities in the vesicles (0.125–2 mol % fractions). The measurement baseline denotes the fabricated streptavidin receptor-modified SLB platform. Vesicles were added from 5 min, and then a buffer rinsing step was conducted from 65 min. (B) Tabulated $\Delta\lambda_{\max}$ shifts for vesicle attachment at saturation and (C) slopes of the $\Delta\lambda_{\max}$ shift responses during the initial attachment stage, plotted on a \log_2 scale and corresponding to the data in panel A. Where applicable, the measurement values are represented by the mean \pm standard deviation from three runs per condition.

supported lipid bilayer (SLB) platform that recapitulates basic architectural features of cell membranes, including membrane-associated receptor presentation. Our experimental strategy was centered around an indirect nanoplasmonic sensing approach, whereby a receptor-modified SLB platform was fabricated upon a silica-covered substrate containing hidden, plasmonic silver nanodisk transducers and real-time attachment and deformation of different-size lipid vesicle populations binding to the SLB were tracked by monitoring changes in the localized surface plasmon resonance (LSPR) measurement signal.²² We interpreted the LSPR experimental data with refined analytical models to extract key structural information about the contact radius and height of attached vesicles in the deformed state, which allowed us to gain quantitative insight into how membrane curvature affects energetic aspects related to membrane bending energy. Through these integrated experimental and theoretical efforts, a major effect of <100 nm membrane curvature on modulating the membrane bending properties of lipid vesicles was identified.

Figure 1A outlines the basic steps involved in the attachment of ligand-modified, membrane-enveloped nanoparticles to receptor-functionalized cell membranes as follows: (1) diffusion toward the cell membrane, (2) binding to cell surface receptors, (3) subsequent nanoparticle reshaping upon attachment, especially in multivalent binding cases, and (4) nanoparticle–membrane fusion or nanoparticle endocytosis depending on the internalization pathway, if applicable. In general, more ligand–receptor binding events between a flexible nanoparticle and a cell membrane surface increase the total magnitude of the binding energy, which can result in more extensive deformation of a bound nanoparticle (Figure 1B). In line with these biological principles, we fabricated an SLB platform that contained a fixed density of membrane-associated streptavidin protein receptors (biotin–streptavidin complexes), which was controlled by including 1 mol % biotinylated lipid in the SLB, and streptavidin proteins could bind to the SLB via biotin–streptavidin coupling. The SLB platform has proven to be useful in various contexts to investigate multivalent ligand–receptor interactions involving biomimetic and biological nanoparticles,^{3,23–29} and we focus here on scrutinizing the nanoparticle size factor, which is a new dimension that benefits from the fabrication control afforded by working with synthetic lipid vesicles.

In addition to controlling the lipid vesicle size, we also tuned the biotinylated lipid fraction (i.e., ligand density) in the

vesicles, whereby the corresponding fraction in 60, 130, or 180 nm diameter vesicles was increased from 0.016, 0.031, or 0.125 mol %, respectively, to 2 mol %. The major phospholipid component in the SLB and vesicles was the 1,2-dioleoyl-*sn*-glycero-3-phosphocholine (DOPC) lipid, and the minor phospholipid component was the 1,2-dioleoyl-*sn*-glycero-3-phosphoethanolamine-*N*-(cap biotinyl) (DOPE-biotin) lipid, which has a biotin-functionalized headgroup. Accordingly, biotinylated lipid vesicles with different biotin fractions were fabricated by the extrusion method and the vesicle populations had average diameters (60, 130, or 180 nm) depending on the extrusion pore size, as measured by dynamic light scattering (DLS) measurements.

Figure 1C presents representative, step-by-step LSPR measurement runs, including SLB fabrication on a silica-coated sensor chip, addition of streptavidin protein to biotinylated lipids in the SLB, and the addition of biotinylated lipid vesicles containing 1 mol % biotin, for different-size vesicle cases. In the LSPR measurements, time-resolved shifts in the peak extinction wavelength of the plasmonic nanodisks, $\Delta\lambda_{\max}$, were tracked by ultraviolet–visible spectroscopy measurements and corresponded to changes in the local refractive index adjacent to the SLB-coated sensor surface, which arose from vesicle attachment and attachment-related deformation.^{30,31} A larger $\Delta\lambda_{\max}$ shift can occur due to greater adsorption uptake and/or more extensive vesicle deformation depending on the context. It is noteworthy that the decay length of the LSPR-enhanced electromagnetic field is on the order of 10–15 nm whereby the relative spatial proximity of lipid molecules within attached vesicles influences the $\Delta\lambda_{\max}$ shift.³²

The SLB platform was fabricated using lipid bicelles, and LSPR measurement tracking showed two-step formation kinetics along with final $\Delta\lambda_{\max}$ shifts of around 3.14 ± 0.13 nm relative to the baseline, both of which are consistent with past reports^{33,34} (Figure S1). Then, streptavidin protein was added to the SLB platform via biotin–streptavidin coupling. Because the biotinylated lipid fraction in the SLB was 1 mol % in all cases, the amount of streptavidin protein receptors attached to the SLB was consistent across all experiments and the corresponding $\Delta\lambda_{\max}$ shift was 0.66 ± 0.10 nm for that step, which also agrees with past reports.²²

Next, biotinylated lipid vesicles were added, which led to a further increase in the $\Delta\lambda_{\max}$ shift due to the attachment of vesicles to membrane-associated streptavidin receptors, and

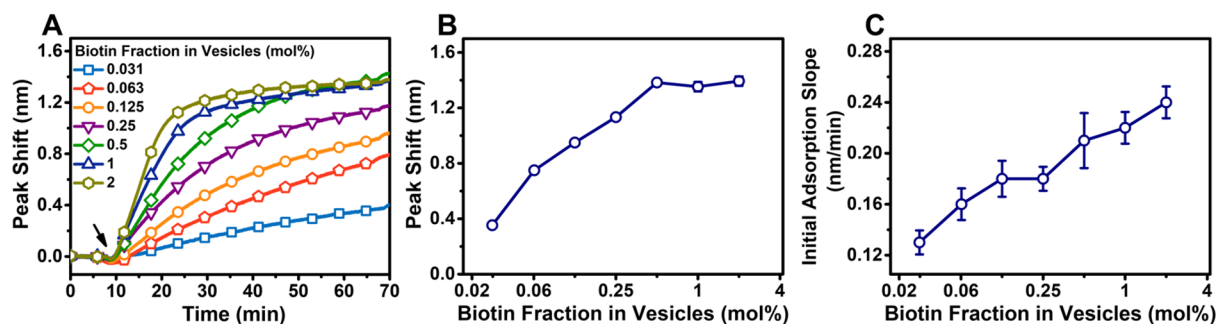


Figure 3. LSPR measurements tracking the attachment of 130 nm diameter, ligand-functionalized vesicles to receptor-functionalized SLBs. As in Figure 2, except that the biotin ligand density in the vesicles ranged from 0.031 to 2 mol % fraction.

the corresponding magnitude of the measurement response depended on the vesicle size and biotinylated lipid fraction in the vesicles. We also confirmed that the biotinylated lipid vesicles of all tested sizes attach specifically to the streptavidin receptors and do not adsorb nonspecifically onto the SLB platform; the specific binding was verified by first incubating the streptavidin-functionalized SLB with free biotin molecules, before the addition of biotinylated lipid vesicles of different sizes (Figure 1D). In those control experiments, the streptavidin receptors were occupied with free biotin molecules so vesicle attachment did not occur, as indicated by nearly negligible changes in the $\Delta\lambda_{\max}$ shifts upon addition of vesicles. On the basis of this platform, we focus on scrutinizing the vesicle attachment kinetics across various biotinylated lipid fractions in the lipid vesicles for the different-size vesicle populations. The measurement baselines in Figures 2–4 correspond to the fabricated SLB platform, i.e., the streptavidin receptor-modified lipid bilayer coating on the sensor surface, and the presented $\Delta\lambda_{\max}$ shifts described below are related to the subsequent vesicle addition step whereby biotinylated lipid vesicles attached to the SLB in a manner dependent on the biotin ligand density in the vesicles and the vesicle size.

Figure 2A shows the time-dependent $\Delta\lambda_{\max}$ shift responses corresponding to the attachment of 60 nm diameter vesicles to an SLB that contained streptavidin receptors. The ligand density was controlled by adjusting the molar fraction of biotinylated lipids in the vesicles from 0.125 to 2 mol %. Across all tested ligand densities, monotonic attachment of intact vesicles was observed on the basis of the measurement signatures and the resulting $\Delta\lambda_{\max}$ shifts at saturation were greater at higher biotin fractions. In the case of vesicles containing 0.125 mol % biotin, the final $\Delta\lambda_{\max}$ shift was 0.89 ± 0.08 nm, and a larger $\Delta\lambda_{\max}$ shift of $\sim 1.19 \pm 0.01$ nm was recorded for vesicles containing 0.25 mol % biotin (Figure 2B). When the biotin fraction in the vesicles was increased to 0.5 mol %, the $\Delta\lambda_{\max}$ shift at saturation was again larger and equal to $\sim 1.45 \pm 0.05$ nm. For vesicles containing 0.75, 1, and 2 mol % biotin fractions, modestly larger $\Delta\lambda_{\max}$ shifts corresponding to 1.65 ± 0.07 , 1.69 ± 0.02 , and 1.68 ± 0.01 nm, respectively, were recorded and indicate that the measurement response began to plateau at higher biotin fractions.

The slope of the $\Delta\lambda_{\max}$ shift during initial vesicle attachment was also calculated, which reflects the degree of vesicle deformation and could be related to the biotin ligand density in the vesicles (Figure 2C). Because the vesicle size was fixed at ~ 60 nm diameter independent of the biotin fraction, the diffusion-limited rate of vesicle attachment was constant and therefore larger initial slopes can be attributed to more

extensive vesicle deformation.^{35,36} The slopes had larger magnitudes when the vesicles had a greater biotin ligand density. At low biotin fractions of 0.125 and 0.25 mol %, the corresponding slopes were $\sim 0.21 \pm 0.03$ and $\sim 0.22 \pm 0.01$ nm/min, respectively. Moreover, for vesicles containing 0.5 mol % biotin, the slope was $\sim 0.33 \pm 0.05$ nm/min, which indicates more extensive vesicle deformation. For vesicles containing 0.75 and 1 mol % biotin, the slopes increased modestly to 0.37 ± 0.02 and 0.39 ± 0.01 nm/min, respectively. Moreover, the slope further increased to 0.47 ± 0.03 nm/min in the case of vesicles containing 2 mol % biotin. Accordingly, we determined that a greater biotin fraction in the vesicles, i.e., a greater ligand density, induces more extensive vesicle deformation and, in turn, a larger $\Delta\lambda_{\max}$ shift at saturation, which agrees well with our past findings for 70 nm diameter vesicles.²²

Figure 3A shows the time-dependent $\Delta\lambda_{\max}$ shift responses corresponding to the attachment of 130 nm diameter vesicles to an SLB that contained streptavidin receptors. The molar fraction of biotinylated lipids in the vesicles was varied from 0.031 to 2 mol %. Again, monotonic vesicle attachment occurred in all cases, and the corresponding $\Delta\lambda_{\max}$ shifts at saturation also tended to be larger at higher biotin fractions. In the case of vesicles containing 0.031 mol % biotin, the final $\Delta\lambda_{\max}$ shift was 0.35 ± 0.03 nm (Figure 3B). For vesicles containing 0.063 and 0.125 mol % biotin, the $\Delta\lambda_{\max}$ shifts increased to 0.75 ± 0.01 and 0.95 ± 0.02 nm, respectively. A larger $\Delta\lambda_{\max}$ shift of $\sim 1.13 \pm 0.02$ nm was observed in the case of vesicles containing 0.25 mol % biotin. Markedly larger $\Delta\lambda_{\max}$ shifts of 1.38 ± 0.01 , 1.35 ± 0.03 , and 1.39 ± 0.03 nm were recorded for vesicles that contained 0.5, 1, and 2 mol % biotin fractions, respectively, indicating a plateau in the measurement response.

The initial slope in the $\Delta\lambda_{\max}$ shift response was again evaluated, and as with the smaller vesicles, the trend indicated that there was more extensive deformation of attached vesicles at higher biotin fractions, especially in the >0.25 mol % biotin regime (Figure 3C). In the case of vesicles containing 0.031 mol % biotin, the slope was $\sim 0.13 \pm 0.01$ nm/min, while the slope increased slightly to 0.16 ± 0.01 nm/min for vesicles containing 0.063 mol % biotin. The slope further increased to $\sim 0.18 \pm 0.01$ nm/min for vesicles containing 0.125 and 0.25 mol % biotin. On the contrary, for vesicles containing 0.5 mol % biotin, the rate increased modestly to 0.21 ± 0.02 nm/min and the slope increased more appreciably to 0.22 ± 0.01 and 0.24 ± 0.01 nm/min for vesicles containing 1 and 2 mol % biotin, respectively.

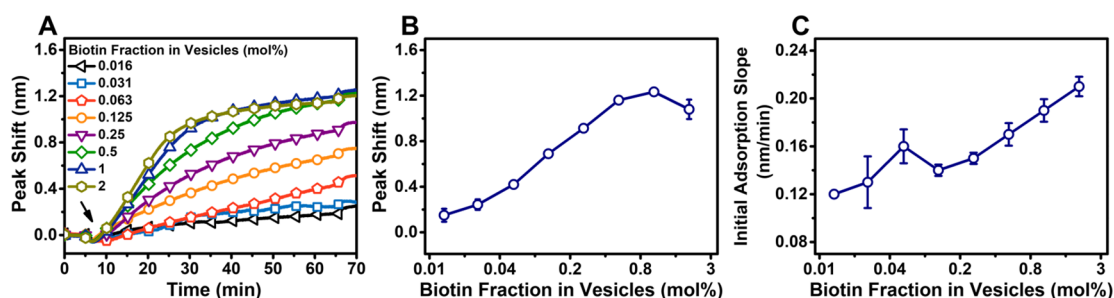


Figure 4. LSPR measurements tracking the attachment of 180 nm diameter, ligand-functionalized vesicles to receptor-functionalized SLBs. As in Figure 2, except that the biotin ligand density in the vesicles ranged from 0.016 to 2 mol % fraction.

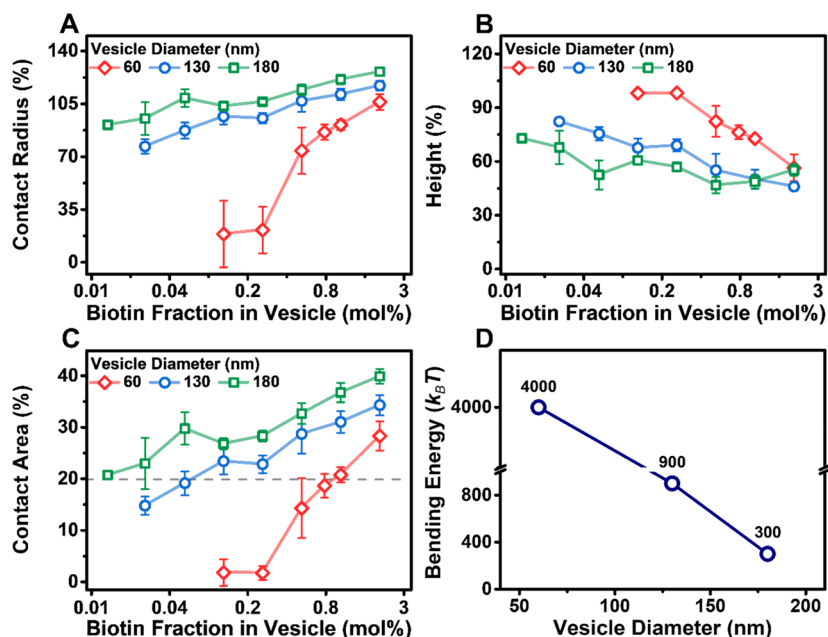


Figure 5. Quantitative analyses of vesicle shape deformation and membrane bending energy for different-size vesicles. All of the results were calculated by using the LSPR data shown in Figures 2C–4C. (A) Normalized radius, r/R , of the attached vesicle region that contacts the SLB platform for different-size vesicles depending on the biotin ligand density (on a \log_2 scale) in the vesicles. (B) Normalized height, $h/2R$, of an attached vesicle corresponding to the data in panel A. (C) Fraction of vesicle surface area contacting the SLB platform, expressed in terms of the relative percentage of total vesicle surface area. The dashed gray line corresponds to an $\cong 20\%$ contact area for comparison. (D) Membrane bending energy for each vesicle size that corresponds to the biotin fraction at which the vesicle contact area percentage is 20% (estimated using the data in panel C and assuming the role of osmotic pressure to be minor).

Figure 4A shows the time-dependent $\Delta\lambda_{\max}$ shift responses corresponding to the attachment of 180 nm diameter vesicles to an SLB that contained streptavidin receptors. In this case, the molar fraction of biotinylated lipids in the vesicles was varied from 0.016 to 2 mol %. For vesicles containing 0.016 and 0.031 mol % biotin, the $\Delta\lambda_{\max}$ shifts were 0.15 ± 0.06 and 0.24 ± 0.05 nm, respectively (Figure 4B). The magnitude of the $\Delta\lambda_{\max}$ shifts steadily increased to 0.42 ± 0.02 , 0.69 ± 0.01 , and 0.91 ± 0.01 nm for vesicles that contained 0.063, 0.125, and 0.25 mol % biotin, respectively. On the contrary, in the case of vesicles containing 0.5 mol % biotin, the $\Delta\lambda_{\max}$ shift increased appreciably to 1.16 ± 0.03 nm, while there were similar $\Delta\lambda_{\max}$ shifts of 1.23 ± 0.02 and 1.08 ± 0.09 nm for vesicles containing 1 and 2 mol % biotin, respectively.

We next determined the initial slopes in the $\Delta\lambda_{\max}$ shift responses, and the trend again showed that there was greater deformation of attached vesicles for vesicles that contained more biotinylated lipids, especially in the >0.5 mol % biotin regime (Figure 4C). The slopes in the $\Delta\lambda_{\max}$ shifts were ~ 0.12 and $\sim 0.13 \pm 0.02$ nm/min for vesicles containing 0.016 and

0.031 mol % biotin, respectively, while slightly larger slopes of $\sim 0.16 \pm 0.01$, $\sim 0.14 \pm 0.01$, and $\sim 0.15 \pm 0.01$ nm/min occurred for vesicles that contained 0.063, 0.125, and 0.25 mol % biotin, respectively. The slope increased slightly to 0.17 ± 0.01 nm/min in the case of vesicles containing 0.5 mol % biotin and further increased to 0.19 ± 0.01 and 0.21 ± 0.01 nm/min for vesicles containing 1 and 2 mol % biotin, respectively.

To analyze the LSPR data for different-size vesicle populations, we refined an analytical model to describe how the $\Delta\lambda_{\max}$ signal is related to the degree of vesicle deformation and could extract shape parameters related to how an attached vesicle contacts the SLB (section 2 of the Supporting Information; see also Figure S2). In our previous study²² in which only small vesicles were studied and the vesicle deformation was considered modest, a deformed vesicle was modeled as a truncated sphere that has a basement of radius r and it was assumed that the radius of a truncated vesicle, R_v , was roughly equal to that of a nondeformed vesicle, R . In the study presented here, we used a wider range of vesicle sizes,

and because larger vesicles can typically undergo more pronounced shape deformation, we adjusted our model of the vesicle shape for analytical calculations. Specifically, R_v was expressed via r and R : $R_v = (4R^2 - r^2)/\sqrt{16R^2 - 8r^2}$. As such, the LSPR measurement response corresponding to diffusion-limited vesicle adsorption can be written as

$$\Delta\lambda_{\max} = B \left[2a \left(\frac{4R^2 - r^2}{\sqrt{16R^2 - 8r^2}} \right) + r^2 \right] C_v t \quad (1)$$

where B is a constant related to the experimental conditions and sensor properties, a is the LSPR-enhanced field penetration depth, C_v is the bulk vesicle concentration, and t is the time elapsed since vesicle attachment began. The time derivative of the LSPR measurement response during the initial stage of vesicle attachment, i.e., the slope, can be further analyzed and described as

$$\frac{\Delta\lambda_{\max}}{\Delta t} \simeq \frac{d\lambda_{\max}}{dt} = B \left[2a \left(\frac{4R^2 - r^2}{\sqrt{16R^2 - 8r^2}} \right) + r^2 \right] C_v \quad (2)$$

Because the values of all of the other parameters in this equation except for r are known or can be determined independently, it is possible to extract the corresponding r values from the experimentally measured slopes described above.

Figure 5A presents the normalized radius, r/R , of the vesicle region (i.e., basement radius) that contacts the SLB platform for different-size vesicles as a function of the biotin ligand density in the vesicles. In all tested cases, there was a similar trend indicating that the contact radius became larger at higher biotin fractions in the vesicles. In the case of 60 nm vesicles, the normalized value of the contact radius of an attached vesicle was $\sim 19\%$ for vesicles containing 0.125 mol % biotin and increased to $\sim 106\%$ for vesicles containing 2 mol % biotin. On the contrary, in the case of 130 nm vesicles that contained biotin fractions ranging from 0.031 to 2 mol %, the normalized contact radius increased from $\sim 77\%$ to $\sim 117\%$. For 180 nm vesicles, the corresponding biotin fraction range in the vesicles was 0.016–2 mol %, and the normalized contact radius increased from $\sim 91\%$ to $\sim 126\%$ across this range. These trends support the idea that the degree of vesicle deformation was generally greater for larger vesicles. At the same time, the magnitude of the change in vesicle deformation from low to high biotin fractions was greatest for small vesicles while larger vesicles had already undergone extensive deformation at relatively low biotin fractions.

On the basis of the calculated contact radius values, we also determined the height of attached, deformed vesicles, h , to further analyze the attachment-induced structural changes in a vesicle. The height of the truncated part of a sphere can be written as $h' = R_v[1 - \cos(\theta)]$, where $\theta = \arcsin(r/R_v)$ is the angle characterizing the truncation. Accordingly, the height of a deformed vesicle was estimated as $2R - h'$. Figure 5B presents the normalized height, $h/2R$, of an attached vesicle as a function of biotin ligand density in the vesicles, for all vesicle sizes. For 60 nm vesicles, the relative height of an attached vesicle decreased from $\sim 98\%$ to $\sim 56\%$ when the ligand density increased from 0.125 to 2 mol % biotin. For 130 and 180 nm vesicles, the relative height of an attached vesicle decreased from $\sim 82\%$ to $\sim 46\%$ and from $\sim 73\%$ to $\sim 55\%$ when the ligand density increased from 0.031 to 2 mol % biotin and

from 0.016 to 2 mol % biotin, respectively. Accordingly, across all tested vesicle sizes, the relative vesicle height decreased when the biotin ligand density in the vesicles was greater. On the contrary, the magnitude of the change in vesicle height was more appreciable for smaller vesicles from low to high biotin fractions, whereas the larger vesicles were already quite deformed even at low biotin fractions.

Taking into account the fact that the total vesicle surface area is $4\pi R^2$ and conserved, we also estimated the corresponding surface area fraction that contacts the SLB, πr^2 , as a function of biotin ligand density in the vesicles, for all vesicle sizes (Figure 5C). In general, this fraction tended to increase at higher biotin fractions for all tested vesicle sizes. For 60 nm vesicles, the corresponding percentage increased from $\sim 2\%$ for vesicles containing 0.125 mol % biotin to $\sim 28\%$ for vesicles containing 2 mol % biotin. On the contrary, for 130 and 180 nm vesicles, the contact area percentage increased from $\sim 15\%$ to $\sim 34\%$ and from $\sim 21\%$ to $\sim 40\%$, respectively, when the biotin fraction increased from 0.031 to 2 mol % or from 0.016 to 2 mol %. In previous works,^{22,24,37} we had determined that a significant degree of vesicle deformation occurred when the contact area percentage reached 10% and, on the basis of this metric, significant vesicle deformation occurred in the case of 130 and 180 nm vesicles even at low biotin fractions.

To quantitatively evaluate how vesicle size affects membrane nanomechanical properties, we estimated the membrane bending energy for each vesicle size that corresponds to the biotin fraction at which the contact area percentage is $\sim 20\%$ (Figure 5D). For 60 nm vesicles, this contact percentage occurred for vesicles containing 1 mol % biotin (defined as $f = 0.01$ on the basis of the fractional quantity of biotinylated lipids relative to all lipids in a vesicle). Accordingly, the number of biotin pairs formed between an attached vesicle and the SLB was estimated to be ≤ 188 when $f \leq 0.01$ (section 3 of the Supporting Information). The change in the total Gibbs free energy, ΔG , that is caused by biotin–streptavidin bond formation (equivalent to 18 kcal/mol) along with the corresponding entropic loss can be calculated with the equation $\Delta G = 18 - 2k_B T \ln(f)$, where k_B is the Boltzmann constant and T is the temperature. The corresponding free energy due to the formation of a biotin–streptavidin pair is ~ 12.5 kcal/mol. For 188 pairs, the increase in Gibbs free energy is ~ 2350 kcal/mol = $4000 k_B T$, which is expected to be comparable to the membrane bending energy and accordingly can be identified as a measure of the latter energy [at least for 60 and 130 nm sized vesicles (see below)] provided the role of the osmotic pressure is minor. Following this approach, for 130 and 180 nm vesicles, the biotin fractions in the vesicles corresponding to a 20% contact area percentage were 0.063 and 0.016 mol %, respectively. From these values, it was determined that the membrane bending energy values corresponding to a 20% contact area percentage were 900 and $300 k_B T$ for 130 and 180 nm vesicles, respectively. Together, these findings support the idea that, when undergoing receptor-mediated shape deformation to an appreciable extent, smaller vesicles have greater opposing membrane bending energies than larger vesicles²¹ (see also ref 38 for detailed analysis) and a sharp transition in the membrane bending energy occurred in the <100 nm diameter range.

Considering that the membrane bending energy and deformation-induced osmotic pressure contribute to vesicle

stiffness, we additionally estimated the osmotic pressure across the lipid bilayer of an attached vesicle (section 4 of the Supporting Information). More specifically, when a vesicle undergoes deformation, the effective ion concentration inside the vesicle increases due to the fixed number of ions and compressed volume while the ion concentration in the bulk solution remains the same and is hence lower than that inside the vesicle. The corresponding scale of the change in the osmotic pressure-related energy due to attachment-related vesicle deformation is given by

$$\Delta E_{\text{op}} = k_{\text{B}}TcV_0(1 - \alpha)^2 \quad (3)$$

where c ($= c_{\text{Na}^+} = c_{\text{Cl}^-}$) is the NaCl concentration in a nondeformed vesicle and in the bulk solution under isotonic conditions, $V_0 = 4\pi R^3/3$ is the volume of a nondeformed vesicle, and α is a dimensionless coefficient characterizing the extent of vesicle deformation that is given by V_{d}/V_0 , where V_{d} is the volume of a deformed vesicle.

Using eq 3, we estimated the trend in how the osmotic pressure-related energy depended on the biotin ligand density in the vesicles, for each vesicle size. For 60 nm diameter vesicles, the osmotic pressure energy was negligible at low biotin ligand densities in the vesicles and reached ~ 60 and $\sim 240 k_{\text{B}}T$ for vesicles containing 1 and 2 mol % biotin, respectively. By contrast, the membrane bending energy was on the order of $4000 k_{\text{B}}T$ for vesicles that contained 1 mol % biotin, indicating that the membrane bending energy, not the osmotic pressure energy, was the major factor influencing vesicle stiffness in this size regime. On the contrary, for larger, 130 nm diameter vesicles, the osmotic pressure energy was ~ 400 and $\sim 1000 k_{\text{B}}T$ for vesicles containing 0.063 and 0.125 mol % biotin, respectively, whereas the corresponding membrane bending energy was on the order of $\sim 900 k_{\text{B}}T$ for vesicles that contained 0.063 mol % biotin. This finding indicates that, as receptor-mediated vesicle deformation became more appreciable, the osmotic pressure energy became the more dominant factor in this case. For the largest, 180 nm diameter vesicles, the osmotic pressure energy was estimated to be even higher, on the order of $\sim 1600 k_{\text{B}}T$, for vesicles that contained 0.016 mol % biotin, whereas the corresponding membrane bending energy was $\sim 300 k_{\text{B}}T$. Hence, for <100 nm vesicles, the membrane bending energy was the major factor influencing vesicle stiffness while the osmotic pressure energy was mainly the dominant factor for larger vesicles, especially in cases of greater receptor-mediated deformation at high biotin fractions in the vesicles (as schematically shown in Figure S3).

In this study, an indirect nanoplasmonic sensing approach was applied to track the attachment and resulting shape deformation of different-size, biotinylated lipid vesicles to a streptavidin receptor-modified, cell membrane-mimicking platform. By combining this LSPR-based experimental approach with analytical modeling to quantify shape parameters related to vesicle deformation, including the contact radius, contact area, and height, we can draw several conclusions about the size-dependent effects on receptor-mediated lipid vesicle attachment and deformation in multivalent ligand–receptor interaction contexts. (i) For all tested vesicle sizes (~ 60 – 180 nm diameter), the vesicle–SLB contact radius percentage increased and the vesicle height decreased for higher biotin fractions in the vesicles, which can be rationalized by a larger binding interaction energy due to more streptavidin–biotin binding events. (ii) At relatively low biotin ligand densities in

the vesicles, larger vesicles already underwent appreciable attachment-related deformation while a higher biotin ligand density in the vesicles was required to induce extensive deformation for smaller vesicles. (iii) The corresponding magnitude of the membrane bending energy opposing appreciable vesicle deformation (i.e., when 20% of the vesicle surface area was located close to the SLB) increased sharply and nonlinearly with a decrease in vesicle size. (iv) The relative interplay of the membrane bending energy and osmotic pressure energy factors contributing to vesicle stiffness occurred in a highly size-dependent manner. For 60 nm diameter vesicles, the membrane bending energy was the dominant factor influencing vesicle stiffness while the osmotic pressure energy was more dominant for 130 and 180 nm diameter vesicles. Collectively, these findings indicate that pronounced changes in the nanomechanical properties of lipid vesicles occur in the <100 nm regime; i.e., for highly curved membranes, there is appreciable membrane stiffening, due to a large membrane bending energy, whereby more extensive multivalent ligand–receptor binding interactions are needed to induce a high degree of vesicle shape deformation compared to larger vesicles with less membrane curvature.

From a biological perspective, our finding that ~ 100 nm membrane curvature demarcates a key transition point influencing the degree to which lipid vesicles can undergo shape deformation in response to multivalent ligand–receptor binding interactions offers numerous possible directions for future research. For example, the diameter of membrane-enveloped virus particles is typically ~ 50 – 250 nm and one might consider how virus particle size affects cellular infectivity processes related to multivalent binding and resulting shape deformation. Such biophysical effects could potentially improve our understanding of why enveloped virus particles undergo either membrane fusion or endocytosis during the initial cellular attachment step. From an applied perspective, rationalizing and eventually harnessing these biophysical effects could also prove to be useful for designing tailored LNPs with well-defined membrane compositions and nanoparticle sizes to improve functional performance. As mentioned in the introduction, this research area is currently a high priority for the development of improved vaccine and drug delivery strategies among various possibilities and highlights how emerging insights into the size-dependent membrane bending properties of nanoscale lipid vesicles are practically relevant to translational medicine and biotechnology applications.

■ ASSOCIATED CONTENT

Supporting Information

The Supporting Information is available free of charge at <https://pubs.acs.org/doi/10.1021/acs.jpcllett.2c00090>.

Experimental details, LSPR analytical modeling for vesicle shape deformation, membrane bending energy analysis, and osmotic pressure energy analysis, including Figures S1–S3 (PDF)

■ AUTHOR INFORMATION

Corresponding Authors

Joshua A. Jackman – School of Chemical Engineering and Translational Nanobioscience Research Center, Sungkyunkwan University, Suwon 16419, Republic of Korea; orcid.org/0000-0002-1800-8102; Email: jjackman@skku.edu

Nam-Joon Cho – School of Materials Science and Engineering, Nanyang Technological University, 637553, Singapore; orcid.org/0000-0002-8692-8955; Email: njcho@ntu.edu.sg

Authors

Hyeonjin Park – School of Chemical Engineering and Translational Nanobioscience Research Center, Sungkyunkwan University, Suwon 16419, Republic of Korea; School of Materials Science and Engineering, Nanyang Technological University, 637553, Singapore

Tun Naw Sut – School of Chemical Engineering and Translational Nanobioscience Research Center, Sungkyunkwan University, Suwon 16419, Republic of Korea

Bo Kyeong Yoon – School of Healthcare and Biomedical Engineering, Chonnam National University, Yeosu 59626, Republic of Korea

Vladimir P. Zhdanov – Boreskov Institute of Catalysis, Russian Academy of Sciences, Novosibirsk 630090, Russia; orcid.org/0000-0002-0167-8783

Jin Woong Kim – School of Chemical Engineering, Sungkyunkwan University, Suwon 16419, Republic of Korea; orcid.org/0000-0002-6485-9936

Complete contact information is available at:

<https://pubs.acs.org/10.1021/acs.jpcllett.2c00090>

Notes

The authors declare no competing financial interest.

ACKNOWLEDGMENTS

This work was supported by National Research Foundation of Korea (NRF) grants funded by the Korean government (MSIT) (2020R1C1C1004385 and 2021R1A4A1032782). Schematic illustrations were created with BioRender.com under an academic lab subscription.

REFERENCES

- (1) Gonda, A.; Kabagwira, J.; Senthil, G. N.; Wall, N. R. Internalization of Exosomes through Receptor-Mediated Endocytosis. *Mol. Cancer Res.* **2019**, *17*, 337–347.
- (2) Van Niel, G.; d'Angelo, G.; Raposo, G. Shedding Light on the Cell Biology of Extracellular Vesicles. *Nat. Rev. Mol. Cell Biol.* **2018**, *19*, 213–228.
- (3) Müller, M.; Lauster, D.; Wildenauer, H. H.; Herrmann, A.; Block, S. Mobility-Based Quantification of Multivalent Virus-Receptor Interactions: New Insights into Influenza A Virus Binding Mode. *Nano Lett.* **2019**, *19*, 1875–1882.
- (4) Overeem, N. J.; van der Vries, E.; Huskens, J. A Dynamic, Supramolecular View on the Multivalent Interaction between Influenza Virus and Host Cell. *Small* **2021**, *17*, 2007214.
- (5) Ding, Y.; Williams, N. H.; Hunter, C. A. A Synthetic Vesicle-to-Vesicle Communication System. *J. Am. Chem. Soc.* **2019**, *141*, 17847–17853.
- (6) Langton, M. J.; Keymeulen, F.; Ciaccia, M.; Williams, N. H.; Hunter, C. A. Controlled Membrane Translocation Provides a Mechanism for Signal Transduction and Amplification. *Nat. Chem.* **2017**, *9*, 426–430.
- (7) Hou, X.; Zaks, T.; Langer, R.; Dong, Y. Lipid Nanoparticles for mRNA Delivery. *Nat. Rev. Mater.* **2021**, *6*, 1078–1094.
- (8) Bost, J. P.; Barriga, H.; Holme, M. N.; Gallud, A.; Maugeri, M.; Gupta, D.; Lehto, T.; Valadi, H.; Esbjörner, E. K.; Stevens, M. M.; El-Andaloussi, S. Delivery of Oligonucleotide Therapeutics: Chemical Modifications, Lipid Nanoparticles, and Extracellular Vesicles. *ACS Nano* **2021**, *15*, 13993–14021.
- (9) Camussi, G.; Deregibus, M. C.; Bruno, S.; Cantaluppi, V.; Biancone, L. Exosomes/Microvesicles as a Mechanism of Cell-to-Cell Communication. *Kidney Int.* **2010**, *78*, 838–848.
- (10) Théry, C.; Ostrowski, M.; Segura, E. Membrane Vesicles as Conveyors of Immune Responses. *Nat. Rev. Immunol.* **2009**, *9*, 581–593.
- (11) Costa-Silva, B.; Aiello, N. M.; Ocean, A. J.; Singh, S.; Zhang, H.; Thakur, B. K.; Becker, A.; Hoshino, A.; Mark, M. T.; Molina, H.; et al. Pancreatic Cancer Exosomes Initiate Pre-metastatic Niche Formation in the Liver. *Nat. Cell Biol.* **2015**, *17*, 816–826.
- (12) Helenius, A. Virus Entry: Looking Back and Moving Forward. *J. Mol. Biol.* **2018**, *430*, 1853–1862.
- (13) Hassett, K. J.; Higgins, J.; Woods, A.; Levy, B.; Xia, Y.; Hsiao, C. J.; Acosta, E.; Almarsson, Ö.; Moore, M. J.; Brito, L. A. Impact of Lipid Nanoparticle Size on mRNA Vaccine Immunogenicity. *J. Controlled Release* **2021**, *335*, 237–246.
- (14) Lee, S. M.; Cheng, Q.; Yu, X.; Liu, S.; Johnson, L. T.; Siegwart, D. J. A Systematic Study of Unsaturation in Lipid Nanoparticles Leads to Improved mRNA Transfection In Vivo. *Angew. Chem., Int. Ed.* **2021**, *60*, 5848–5853.
- (15) Zhang, H.; Freitas, D.; Kim, H. S.; Fabijanic, K.; Li, Z.; Chen, H.; Mark, M. T.; Molina, H.; Martin, A. B.; Bojmar, L.; et al. Identification of Distinct Nanoparticles and Subsets of Extracellular Vesicles by Asymmetric Flow Field-Flow Fractionation. *Nat. Cell Biol.* **2018**, *20*, 332–343.
- (16) Sorkin, R.; Huisjes, R.; Bošković, F.; Vorselen, D.; Pignatelli, S.; Ofir-Birin, Y.; Freitas Leal, J. K.; Schiller, J.; Mullick, D.; Roos, W. H.; et al. Nanomechanics of Extracellular Vesicles Reveals Vesiculation Pathways. *Small* **2018**, *14*, 1801650.
- (17) Vorselen, D.; MacKintosh, F. C.; Roos, W. H.; Wuite, G. J. Competition between Bending and Internal Pressure Governs the Mechanics of Fluid Nanovesicles. *ACS Nano* **2017**, *11*, 2628–2636.
- (18) Li, S.; Eghiaian, F.; Sieben, C.; Herrmann, A.; Schaap, I. A. Bending and Puncturing the Influenza Lipid Envelope. *Biophys. J.* **2011**, *100*, 637–645.
- (19) Vorselen, D.; van Dommelen, S. M.; Sorkin, R.; Piontek, M. C.; Schiller, J.; Döpp, S. T.; Kooijmans, S. A.; van Oirschot, B. A.; Versluijs, B. A.; Bierings, M. B.; et al. The Fluid Membrane Determines Mechanics of Erythrocyte Extracellular Vesicles and is Softened in Hereditary Spherocytosis. *Nat. Commun.* **2018**, *9*, 4960.
- (20) Ridolfi, A.; Brucalè, M.; Montis, C.; Caselli, L.; Paolini, L.; Borup, A.; Boysen, A. T.; Loria, F.; van Herwijnen, M. J.; Kleinjan, M.; et al. AFM-Based High-Throughput Nanomechanical Screening of Single Extracellular Vesicles. *Anal. Chem.* **2020**, *92*, 10274–10282.
- (21) Ye, S.; Li, W.; Wang, H.; Zhu, L.; Wang, C.; Yang, Y. Quantitative Nanomechanical Analysis of Small Extracellular Vesicles for Tumor Malignancy Indication. *Adv. Sci.* **2021**, *8*, 2100825.
- (22) Park, H.; Sut, T. N.; Yoon, B. K.; Zhdanov, V. P.; Cho, N.-J.; Jackman, J. A. Unraveling How Multivalency Triggers Shape Deformation of Sub-100 nm Lipid Vesicles. *J. Phys. Chem. Lett.* **2021**, *12*, 6722–6729.
- (23) Nie, C.; Stadtmüller, M.; Parshad, B.; Wallert, M.; Ahmadi, V.; Kerkhoff, Y.; Bhatia, S.; Block, S.; Cheng, C.; Wolff, T.; Haag, R. Heteromultivalent Topology-Matched Nanostructures as Potent and Broad-Spectrum Influenza A Virus Inhibitors. *Sci. Adv.* **2021**, *7*, eabd3803.
- (24) Di Iorio, D.; Lu, Y.; Meulman, J.; Huskens, J. Recruitment of Receptors at Supported Lipid Bilayers Promoted by the Multivalent Binding of Ligand-Modified Unilamellar Vesicles. *Chem. Sci.* **2020**, *11*, 3307–3315.
- (25) Cawley, J. L.; Jordan, L. R.; Wittenberg, N. J. Detection and Characterization of Vesicular Gangliosides Binding to Myelin-Associated Glycoprotein on Supported Lipid Bilayers. *Anal. Chem.* **2021**, *93*, 1185–1192.
- (26) Di Iorio, D.; Verheijden, M. L.; Van Der Vries, E.; Jonkheijm, P.; Huskens, J. Weak Multivalent Binding of Influenza Hemagglutinin Nanoparticles at a Sialoglycan-Functionalized Supported Lipid Bilayer. *ACS Nano* **2019**, *13*, 3413–3423.

(27) Parveen, N.; Rydell, G. E.; Larson, G. R.; Hytönen, V. P.; Zhdanov, V. P.; Höök, F.; Block, S. Competition for Membrane Receptors: Norovirus Detachment via Lectin Attachment. *J. Am. Chem. Soc.* **2019**, *141*, 16303–16311.

(28) Block, S.; Zhdanov, V. P.; Höök, F. Quantification of Multivalent Interactions by Tracking Single Biological Nanoparticle Mobility on a Lipid Membrane. *Nano Lett.* **2016**, *16*, 4382–4390.

(29) Rodrigo, D.; Tittl, A.; Ait-Bouziad, N.; John-Herpin, A.; Limaj, O.; Kelly, C.; Yoo, D.; Wittenberg, N. J.; Oh, S.-H.; Lashuel, H. A.; Altug, H. Resolving Molecule-Specific Information in Dynamic Lipid Membrane Processes with Multi-Resonant Infrared Metasurfaces. *Nat. Commun.* **2018**, *9*, 2160.

(30) Jackman, J. A.; Zhdanov, V. P.; Cho, N.-J. Nanoplasmonic Biosensing for Soft Matter Adsorption: Kinetics of Lipid Vesicle Attachment and Shape Deformation. *Langmuir* **2014**, *30*, 9494–9503.

(31) Oh, E.; Jackman, J. A.; Yorulmaz, S.; Zhdanov, V. P.; Lee, H.; Cho, N.-J. Contribution of Temperature to Deformation of Adsorbed Vesicles Studied by Nanoplasmonic Biosensing. *Langmuir* **2015**, *31*, 771–781.

(32) Willets, K. A.; Van Duyne, R. P. Localized Surface Plasmon Resonance Spectroscopy and Sensing. *Annu. Rev. Phys. Chem.* **2007**, *58*, 267–297.

(33) Sut, T. N.; Jackman, J. A.; Yoon, B. K.; Park, S.; Kolahdouzan, K.; Ma, G. J.; Zhdanov, V. P.; Cho, N.-J. Influence of NaCl Concentration on Bicelle-Mediated SLB Formation. *Langmuir* **2019**, *35*, 10658–10666.

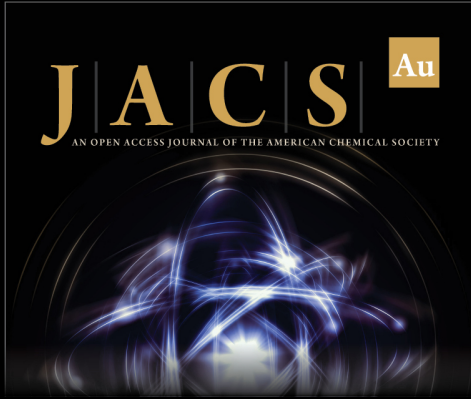
(34) Jackman, J. A.; Cho, N.-J. Supported Lipid Bilayer Formation: Beyond Vesicle Fusion. *Langmuir* **2020**, *36*, 1387–1400.

(35) Jackman, J. A.; Špačková, B.; Linardy, E.; Kim, M. C.; Yoon, B. K.; Homola, J.; Cho, N.-J. Nanoplasmonic Ruler to Measure Lipid Vesicle Deformation. *Chem. Commun.* **2016**, *52*, 76–79.

(36) Jackman, J. A.; Yorulmaz Avsar, S.; Ferhan, A. R.; Li, D.; Park, J. H.; Zhdanov, V. P.; Cho, N.-J. Quantitative Profiling of Nanoscale Liposome Deformation by a Localized Surface Plasmon Resonance Sensor. *Anal. Chem.* **2017**, *89*, 1102–1109.

(37) Zhdanov, V. P. Ligand-Receptor-Mediated Attachment of Lipid Vesicles to a Supported Lipid Bilayer. *Eur. Biophys. J.* **2020**, *49*, 395–400.

(38) Seifert, U. Configurations of Fluid Membranes and Vesicles. *Adv. Phys.* **1997**, *46*, 13–137.



JACS Au
AN OPEN ACCESS JOURNAL OF THE AMERICAN CHEMICAL SOCIETY

Editor-in-Chief
Prof. Christopher W. Jones
Georgia Institute of Technology, USA

Open for Submissions 

pubs.acs.org/jacsau  ACS Publications
Most Trusted. Most Cited. Most Read.